Experimental and numerical study of flood dynamics in a river-network-floodplain set-up

Vijay Kisan Mali, B. Veeranna, Aditya Parik and Soumendra Nath Kuiry

ABSTRACT

Flood simulations demand mathematical models, which are rigorously calibrated and validated against benchmarking datasets. For this purpose, experiments are conducted in a river-network-floodplain set-up. Hypothetical stepped hydrographs are passed through the channel-network, and fluvial flooding situations are created. Flood depths are recorded at various locations and evolving flood extents are extracted by image processing. TELEMAC 2D is tested against the observed data. The most accurate scheme for flood prediction is identified through sensitivity analysis. Inclusion of the turbulence model is found to improve the accuracy in predicting dynamic flood extents. The model seems to slightly overpredict inundation extents during the rising limb of the hydrographs and underpredict during the falling limb. In addition, certain aspects of a flood such as river–floodplain interaction and junction hydraulics cannot be reproduced with high precision by the 2D model. The experimental datasets can be a valuable resource to mathematical modellers and are freely downloadable.

Key words | benchmarking datasets, flood events, numerical modelling, river flood, river-network-floodplain set-up

Vijay Kisan Mali (corresponding author)
B. Veeranna
Soumendra Nath Kuiry
Environmental and Water Resources Engineering
    Division, Department of Civil Engineering,
IIT Madras,
Chennai,
India
E-mail: *vijayagril@gmail.com*

Aditya Parik
Department of Civil Engineering,
IIT Kharagpur,
Kharagpur,
India

INTRODUCTION

Flood modelling has been an active field of research for simulating multifarious aspects of flood flow processes in riverine systems, coastal sites, and urban areas. Reliable prediction of flood is a prerequisite to substantiate contemporary flood risk management policies. This includes accurate estimation of flood extents, depths, and velocities in the areas under interest. Generally, the aforementioned information can be obtained after several hours of simulations that are executed by mathematical models. A variety of such models have been developed over the years (Di Baldassarre *et al.* 2009; Martins *et al.* 2017). However, rapid and accurate flood prediction in a complex topographical setting at higher spatiotemporal resolution remains a great challenge for the models. The complexity of the scenario is increased by greater variations in land-use and built-up infrastructure, non-availability of dataset for model calibration and validation, chaotic nature of flooding, and

uncertainty associated with flood modelling (Teng *et al.* 2017).

Irrespective of the type of the mathematical model, it is important that the performance of the model needs to be assessed against observed datasets for judging the degree of applicability of the underlying governing equations and the numerical schemes to describe the physical processes being modelled. This approach eventually helps in understanding the predictive capability of the model and provides new ways to improve it further (Giustarini *et al.* 2015). Moreover, an investigation of the accuracy of a model further relies on the accuracy of the observed data. Observational flood data from the field, unfortunately, are still rare and inadequate. Also, pre- and post-flooding field measurements usually suffer from high uncertainty and low accuracy as described by Smith *et al.* (2014). Hence, in recent years, remotely sensed data from satellites (Eltner

et al. 2016), most commonly in the form of flooding extent, is used as the only large-scale data for validation of models. Nonetheless, even such data suffer from several uncertainties, and a detailed discussion is presented by Merwade *et al.* (2008) and Schumann *et al.* (2009). As a result, these poor quality datasets become insufficient for a thorough investigation of model performance (Sanyal 2017). There have also been effort to collect crowd-sourced measurements using smartphones to develop a low-cost practical method for model validation (Kampf *et al.* 2018). Recently, Bhola *et al.* (2019) have presented a computer vision algorithm to generate flow depth data from the images, which can be used to validate mathematical models. Despite the aforementioned shortcomings in the datasets, predictions from almost every existing model have been compared to either these datasets or analytical solutions of idealized cases (Nicholson *et al.* 1997) in the absence of any better alternative. Assessments of this kind may be good enough only during the initial stages of model development and when very high accuracy is not warranted. However, further development of mathematical models to better represent flow physics is hampered by the absence of qualitative and quantitative observed datasets. As a result, complex physical processes involved in floods such as river–floodplain interaction and flow dynamics at a river bifurcation and junction still remain as challenging tasks to be reproduced by mathematical models.

To address this lack of data for validation, laboratory experiments, which are easier to control and can provide more complete datasets with minimal uncertainty, can play a constitutive role in the river–floodplain flow modelling. The last few decades have witnessed a surge of laboratory experiments being conducted on floods to collect time series of water level evolution and velocity distribution for validating a variety of numerical models. These datasets primarily focus on: channel–floodplain interaction (Zheleznyakov 1971); dam-break floods (Soares-Frazão & Zech 2007); dam-break floods with movable bed (Qian *et al.* 2018); flash floods in urban cities (Testa *et al.* 2007); river-junction flow (Weber *et al.* 2001); flow and sediment transport in sharp open-channel bends (Zeng *et al.* 2008); and mean flow and turbulence in vegetated open-channel flow (Defina & Bixio 2005). The IMPACT research programme (Soares-Frazão 2007; Soares-Frazão & Zech 2007; Testa

et al. 2007) has taken a major initiative for investigating and generating flood dynamics data. Soares-Frazão & Zech (2007) generated a dataset on dam-break flood influenced by obstacles for investigating the shock-capturing ability of numerical models. Likewise, Testa *et al.* (2007) carried out experiments on the flooding of an urban district model made up of concrete blocks. Over the period, these datasets have been extensively put to the test by many researchers (Soares-Frazão *et al.* 2008; Abderrezzak *et al.* 2009) for evaluating model performance and understanding the underlying physical processes. A few studies have also been reported on river–floodplain flow interaction (Zheleznyakov 1971; Wormleaton & Merrett 1990). However, these experiments considered relatively flat floodplains extending on both banks of a single river channel. Few experimentalists (Wormleaton *et al.* 2004; Shiono *et al.* 2009) have attempted to understand the flow mechanism in meandering channels linked with floodplains. Nevertheless, it is observed that the above experiments are, in general, simple as the considered geometries rarely reflect true ground details. In reality, floods often take place over plain lands and delta regions where the main river forms complicated branched networks, and the flood dynamics become far more complex due to the exchange of flow in a river-network-floodplain system. Therefore, experiments in a river-network-floodplain like system become complicated on account of sinuosity of the channels, and the presence of confluence, bifurcation, islands, channel loops, highlands, and undulating floodplains. Such a complex topography is one of the important factors that affect the flow behaviour and controls the spatial variability of flow magnitude and direction. Mali & Kuiry (2020) have reported the flood dynamics datasets in a river-network-floodplain system during the steady-state flow condition. The datasets represent complex flood dynamics that can be used for investigating the hydrodynamic features and subsequently for model validation. However, to the best of the authors' knowledge, a laboratory data on flood dynamics for such a complex system during the unsteady-state flow condition is not available at the time of writing. The flow dynamics in a river-network-floodplain system during the unsteady-state flow condition would be more challenging for the models to predict accurately. This is because the unsteady nature of flow and the complex flow processes concurrently occur within the system. The

lack of this kind of essential experimental data certainly impedes model validation and also the selection of a suitable model (e.g. one-dimensional (1D), two-dimensional (2D), coupled 1D–2D, or three-dimensional (3D)) considering simulation time and accuracy. Thus, in view of these limitations and usefulness of the data, the present research aims in generating benchmarking datasets on flood dynamics in a river-network-floodplain set-up during the unsteady-state flow condition with the help of state-of-the-art sensors and the image processing technique.

Apart from generating datasets by conducting laboratory experiments, this study also focuses on applicability of the observed datasets to validate a numerical model, TELEMAC 2D (http://www.opentelemac.org/). This 2D shallow water flow model is chosen based on its strengths such as geometric flexibility, availability of different solution schemes and turbulence closure models and being an open-source code. The model is already successfully applied for several realistic scenarios, including simulations of the flood inundation phenomena. The accuracy is reported within the range from excellent to reasonable (Sanyal *et al.* 2014; Stark *et al.* 2016) for different combinations of hydrodynamic and turbulence closure models. It should be noted that in all the above applications, the model was validated against analytical tests, simplified laboratory experiments, and satellite data. However, in the absence of flood-related experimental dataset, it is impossible to rigorously evaluate the performance of various numerical schemes and turbulence models available in TELEMAC 2D. Hence, the recorded dataset comprises of a combination of dynamic flood inundation extents and corresponding continuous hydrometric variables during the propagation of a flood wave through a channel-network-floodplain system. The dataset can be extremely useful for evaluating the predictive capabilities of a numerical model (Horritt & Bates 2002). Considering this fact, the objectives of the present study are set as follows: (a) conducting physical experiments on floods in a laboratory river-network-floodplain set-up for different flood hydrographs, (b) recording the time series of water levels at various locations and to map the flood extents at intervals of 5 min using the visual image interpretation technique, and (c) evaluating the quality of the benchmarking dataset and flood prediction capability of the TELEMAC2D numerical model.

EXPERIMENTAL AND NUMERICAL METHODS

Laboratory set-up

The experimental set-up is constructed at the hydraulics laboratory of the Indian Institute of Technology (IIT) Madras, India (see Figure 1). This is not a scaled model of a definite field location since the focus is on capturing the flood dynamics along the considerable length of a river-network system, and flow within the river branches, and the hydraulic interaction between river and floodplain flows. The river-network is laid out on a generic topology replicating a typical river-network-floodplain system that is commonly encountered in coastal and inland delta regions. The set-up consists of one confluence and three bifurcations interspersed with islands, mounds, and undulating floodplains. All possible physical constraints and situations are reproduced such as adequate delivery of flow; uniform bed roughness for simplicity; distance required to develop the flow at the inlet; and the draining of flow without affecting the downstream boundary.

The set-up is 20 m long and 5 m wide with a single inlet channel and three outlets at the ends of the three exit branches (see Figure 1). The sharp-crested weirs made of the thin metal plate are placed at the outlets. The depth of the channels from the bank level is about 0.2 m with an average bed slope of 1 : 1,000 from upstream to downstream.

Figure 1 | Laboratory river-network-floodplain set-up looking downstream from the inlet channel.

The entire surface is finished with smooth concrete. The pipe framework visible in Figure 1 has its horizontal members located at 3.5 m above the channel bed and is used to mount the cameras and sensors. Further details about the set-up are elaborated in Mali & Kuiry (2018).

Data acquisition and experimental procedure

The experimental datasets are acquired in two steps. First, the overlapping images of the set-up are captured and precise ground control points (GCPs) are surveyed using the total station instrument under the dry condition. This information is used to create a very high-resolution (1 mm grid) 3D topography (see Figure 2) and the ortho-image of the set-up. For this process, the structure-from-motion (SfM) and multi-view stereo (MVS) photogrammetry techniques available in the PhotoScan software (https://www.agisoft.com) are used. The accuracy of the reconstructed topography of the set-up is found to be within ±3.45 mm. The detailed explanation of the image processing protocol is reported by Mali & Kuiry (2018). This 3D topography is used for generating the computational mesh for numerical simulations.

In the second step, flow depths and images of the flooded set-up are acquired during each experimental run. Each run commences by opening the inlet valve, allowing water to flow into the dry main channel. Minimum flow is maintained to ensure that all the channels are wet and flow depths are just above the weirs at the outlets. This also ensures that any formation of back surge or drastic flow acceleration, especially during the initial opening of the inlet sluice valve, is avoided. As the inflow rate is increased with time, the water level in the channels rises gradually, exceeding the bank levels at the low points and resulting in flooding of the hinterland. For generating such flood conditions, three unsteady-state stepped hydrographs (see Figure 3(a)) are introduced at the inlet by regulating the sluice valve. The valve operation was achieved after several trials and by controlling the opening aperture at different times. The unsteady flow through the inlet is measured by an electromagnetic flowmeter fitted in the supply pipe after the sluice valve. The time to peak, peak discharge, and base of each inflow hydrograph are different. However, the rising limb of every hydrograph is maintained the same in terms of equal incremental flow rate. The flood depths at different locations are recorded at intervals of 2 s by ultrasonic level sensors.

A total of 17 gauges (6 in the channels and 11 on the floodplains) marked in solid green circles (●) on the ortho-image (see Figure 4) is used to record the time series of flow depth evolution. Due to an insufficient number of ultrasonic sensors, the experiments are repeated twice to collect flow depths at all the gauges.

The experiments are again repeated after removing the sensors so as to capture images of the flooded set-up at intervals of 5 min with sufficient side- and end-lap between two consecutive images. Five digital single-lens reflex (DSLR) cameras with wide angle lens (Tokina 11–16 mm) set on 11 mm focal length and field of view (4.9×7.3) m^2 are used to acquire the images. The images are then processed for retrieving the dynamic flood inundation extents. The accuracy limits of various devices and repeatability of the experiments are discussed in the following sections.
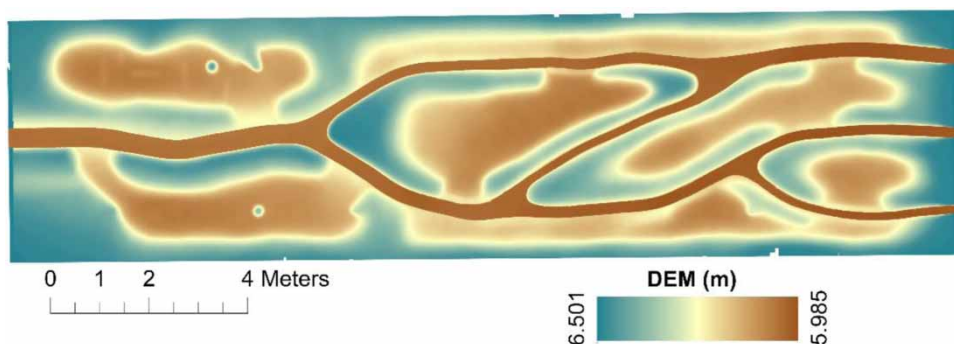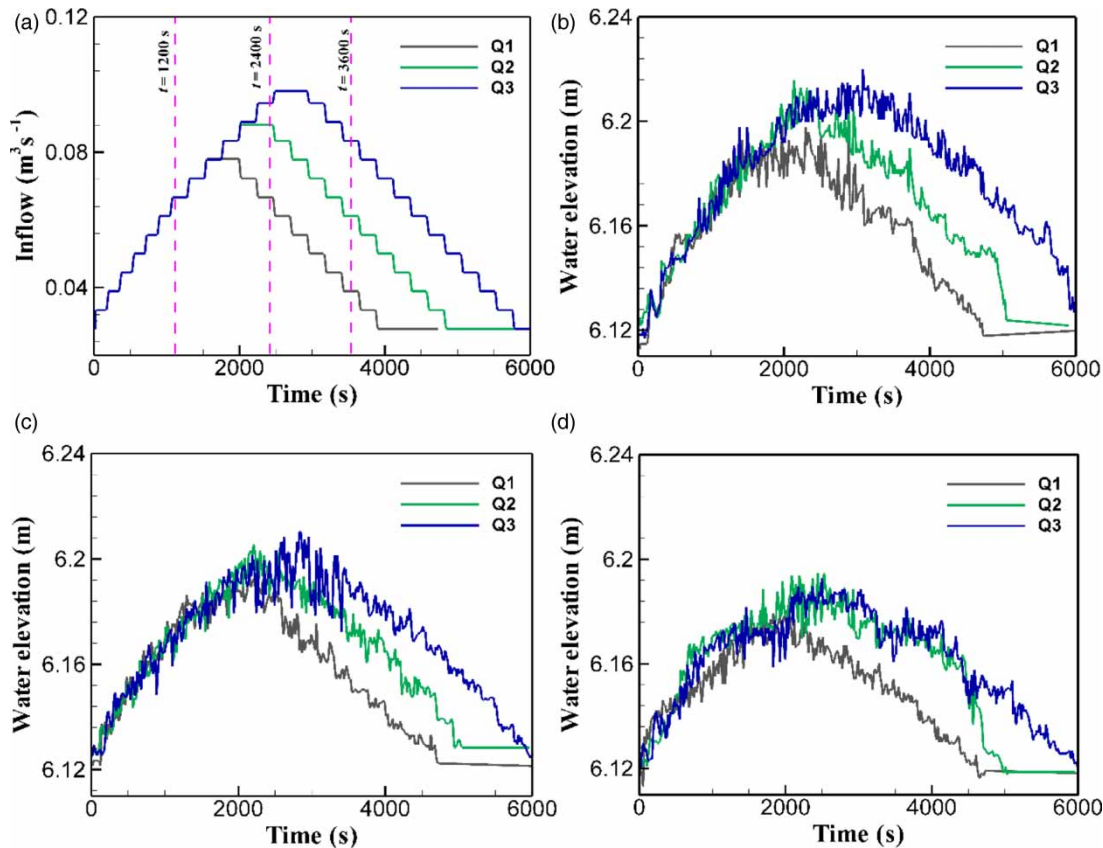

Figure 2 | High-resolution topography of the set-up generated using PhotoScan.

Figure 3 | Boundary conditions: (a) unsteady-state stepped discharge hydrographs (Q1, Q2 and Q3) at the upstream and recorded flow depth evolution at downstream of (b) left channel (c) middle channel, and (d) right channel with respect to the flow direction.

Repeatability

The repeatability of the experiments is tested by conducting the same experiments twice and by comparing flow depths and inundation extents. The repeated runs show good agreement with the earlier datasets. However, it may be admitted that minor differences cannot be avoided. These are likely associated with the randomness of fluctuation of the flow field which may be attributed to the complex topography of the set-up, sensitivity of the instruments, measurement uncertainties, and manual operation of the control valves.

Data accuracy

The total station survey based ground truth data is used for the digital elevation model (DEM) generation and its accuracy assessment. The manufactured accuracy of the instrument is about 2–5 mm within the range of 5 km. The

electromagnetic flowmeter has an accuracy of ±0.5% of displayed reading. The ultrasonic sensors used for this study have a manufactured accuracy of ±2 mm. These sensors use the speed of ultrasound to estimate the distance between the sensor and the water surface, which is temperature-dependent. The sensors are placed in an open laboratory set-up, and hence direct solar radiation occasionally falls on the sensor body, which may cause the rise of internal temperature of the sensors and result in different estimations. There may also be a possibility that ultrasound can be corrupted with noise from background sound, and error may be introduced in the measured values. However, this error is not significant as repeatability shows good agreement for the same inflow hydrograph. As for the cameras used to record the images from above, the internal clocks of all the cameras were accurately synchronized to the Indian Standard Time (IST) for simultaneously capturing the images. However, the variation at the level of a
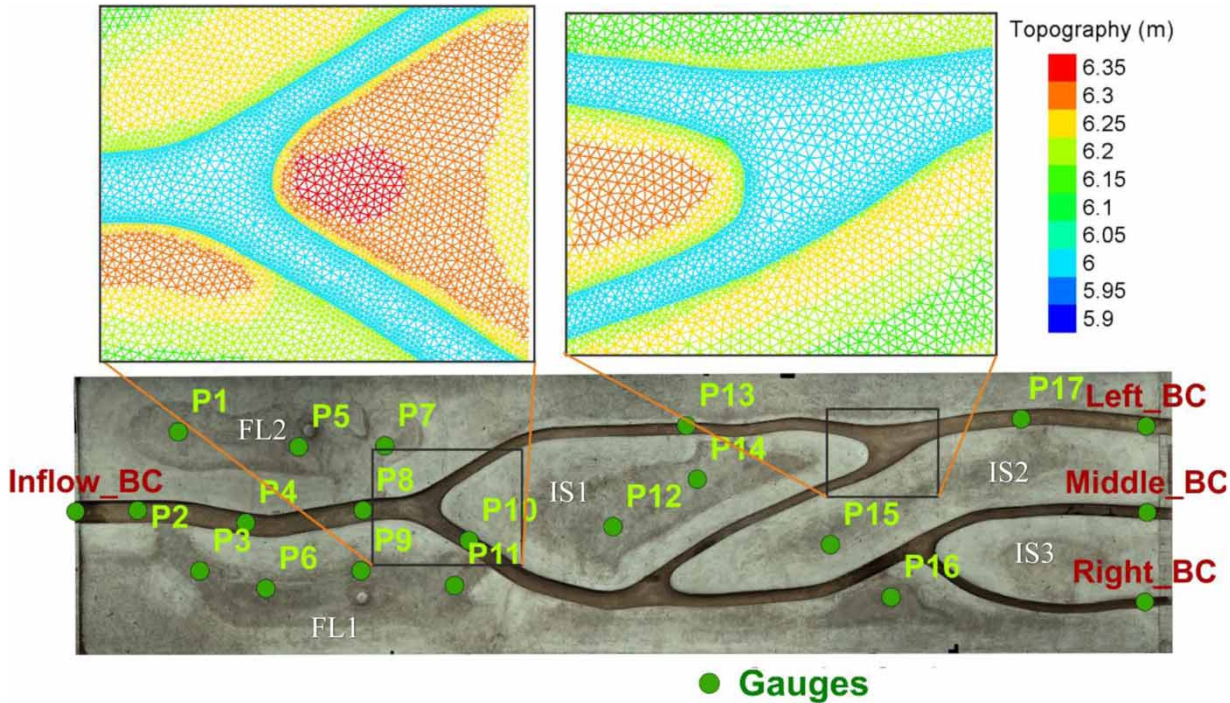
Figure 4 │ Measurement locations of flow depth (gauging stations) within the set-up (FL stands for floodplain and IS stands for island) and locally refined mesh used for numerical modelling. Please refer to the online version of this paper to see this figure in colour: http://dx.doi.org/10.2166/hydro.2020.160.

fraction of a second or a second for taking images cannot be ruled out, and for this, no corrective action is presumed as important.

Numerical modelling

The TELEMAC 2D hydrodynamic model is chosen to simulate the physical processes involved in the experimental study. This model is selected for two reasons: (i) the 2D governing equations are solved by a variety of numerical schemes and (ii) a number of turbulence closure models are also supported by the model (Hervouet & Van Haren 1996). Therefore, the same model platform offers a wide range of solution schemes and the most accurate combination can be identified for further analysis. The 2D depth-averaged Navier–Stokes equations for continuity (1) and momentum (2) and (3) are simultaneously solved in the TELEMAC 2D.

The continuity equation is given as follows:

$$\frac{\partial h}{\partial t} + \vec{u} \cdot \vec{\nabla}(h) + h\,div(\vec{u}) = S_h \tag{1}$$

The momentum equations are given as follows:

$$\frac{\partial u}{\partial t} + \vec{u} \cdot \vec{\nabla}(u) = -g\frac{\partial Z}{\partial x} + S_x + \frac{1}{h}div(hv_t\vec{\nabla}u) \tag{2}$$

$$\frac{\partial v}{\partial t} + \vec{u} \cdot \vec{\nabla}(v) = -g\frac{\partial Z}{\partial y} + S_y + \frac{1}{h}div(hv_t\vec{\nabla}v) \tag{3}$$

where h is the depth of water (m); u and v are the depth-averaged velocity components (m/s) in the x- and y-directions; g is the gravitational acceleration (m/s^2); Z is the free surface elevation (m) above the reference level; t is the time (s); S_h is the source or sink term (m/s); x and y are the horizontal Cartesian coordinates (m); v_t is the momentum diffusion coefficients; and S_x and S_y are the source term (m/s^2).

As said above, several turbulence viscosity models are available in the TELEMAC 2D. However, in this study, the Smagorinsky and k-epsilon (k–ε) turbulence models are selected to understand the importance of turbulence during a flood event. The Smagorinsky turbulence model is a sub-grid scale model for large eddy simulation and is based on the hypothesis that small-scale eddies dissipate

entirely and instantaneously, and receive all the energy from the large scales (Blazek 2015). The energy is transported from the large scales towards the sub-grid scales. The k–ε turbulence model uses two transport equations for calculating the physical quantities that represent the general description of turbulence. The two transport equations are, in general, based on turbulent kinetic energy and the turbulent dissipation rate. This is the most widely used two-equation eddy-viscosity model (Blazek 2015). More details on the k-epsilon model can be found in Blazek (2015).

In this study, we have employed three numerical schemes that are used to solve the above transport equations. A brief description of these schemes is given here. However, the detailed formulation of the various schemes is reported in Hervouet (2007). The three numerical schemes, namely the method of characteristics, centred semi-implicit scheme and the streamline upwind Petrov–Galerkin method (SUPG), and the edge-by-edge implementation of the upwind explicit finite volume method are used in this study to solve the advection terms (Equations (2) and (3)) of TELEMAC 2D. The method of characteristics is unconditionally stable and provides monotonic solution but has two limitations, namely the diffusive nature and the lack of exact mass-conservation. However, the scheme is used for the advection of velocities, and hence, the mass-conservation and monotonicity are of a lesser importance (Hervouet 2013). The SUPG is originally developed by Brooks & Hughes (1982). The SUPG uses the test functions deformed by the direction of flow currents. The test functions are obtained by quadratic functions with the help of the Petrov–Galerkin method. The original SUPG has been modified in TELEMAC 2D to meet the specificities of the equations, so that the unwinding scheme is proportional to the Courant–Friedrichs–Lewy (CFL) condition (Hervouet 2007). The edge-by-edge implementation of the upwind explicit finite volume method is unconditionally stable (Hervouet *et al.* 2011). It is the only scheme in TELEMAC 2D that has improved stability on dry zones, mass-conservation, and monotonicity. However, this implicit scheme can cause the problem of negative depths. This is why a positive depth algorithm is implemented in the post-treatment that ensures both mass-conservation and depth positivity. Further information on the TELEMAC 2D model can be found in the user manual (http://wiki.opentelemac.org/).

The TELEMAC 2D model has been used in several studies, especially those involving field applications in flood-related studies (Barthélémy *et al.* 2018). In addition, the model solves the equations on a flexible unstructured triangular mesh, allowing the user to define any irregular geometry with local refinement. The freely available pre-/post-processing software package Blue Kenue (https://www.nrc-cnrc.gc.ca/eng/solutions/advisory/blue_kenue_index.html) is used to generate the triangular mesh. In the present study, the mesh refinement is performed in the channels, bifurcations, and junction. Smooth transitions are imposed from smaller elements in channels to larger elements over floodplains in order to increase model stability and reduce computation time (see Figure 4). The set-up geometry in the present case is defined by 111,665 elements. The initial condition in the channel-network is imposed as a wet bed by specifying a constant water surface elevation of 6.12 m, i.e. on an average, a flow depth of 0.12 m at the downstream. The initial water surface elevation is kept just above the weir plates positioned at the downstream. The initial flow of the hydrograph at the inlet, i.e. 0.027 m^3/s, is prescribed as an inlet boundary condition, and a constant initial water surface elevation, i.e. 6.12 m, is defined as a downstream boundary condition at the outlets. The boundary conditions are held constant until the flow in the channel-network reaches a steady state, taking approximately 1 h. Once the steady state is attained, the recorded flood hydrographs (see Figure 3(a)) and observed water surface variations (see Figure 3(b)–3(d)) are prescribed at the inlet and three outlets, respectively, to simulate the experimental flood events.

RESULTS AND DISCUSSION

This section describes the evolution of flood depths at different gauges and dynamic flood extents in the experimental set-up. The performance of the 2D numerical model is then examined against the observed dataset through rigorous statistical analysis.

Experimental analysis

Flow depth evolution

Figures 5 and 6 show the flow depth variations in the channels and over the floodplains at different gauges. These figures provide a detailed account of the propagation of water waves, rise, and fall of water levels, and time to reach peak water level at a gauge location.

The maximum flow depths observed in the channels and over the floodplains depend strongly on the location of the gauges. This is also due to complex flow dynamics and wave patterns caused by uneven topography. For instance, in the channels, the maximum flow depths (see Figure 5(b)) at P4 for the different discharges Q1, Q2, and Q3 are observed to be 21.35, 23.55, and 25.10 cm, respectively, despite the channel width and bed roughness being the same along the first stretch of the main channel. This is due to the movement of waves in the opposite direction

after reflection against the divergence wall at bifurcation D1. Apart from that, a weak hydraulic jump is also observed at the upstream of bifurcation D1, and that shock propagates in the reverse flow direction until its intensity diminishes against the inflow discharge. However, the intensity of the jump depends on the magnitude of inflow discharge. The fluctuation in water surface can be seen at P10 (see Figure 5(d)) located just after the bifurcation, D1. Also, at P10, initially the water level rises gradually, and then the rate of rising decreases for a certain period of time, and then again starts rising abruptly to the peak. A very similar trend can also be seen on the recession limb.

Some floodplains act as storages up to its maximum capacity and subsequently become conveyance for higher discharge rate, for example, the floodplain left (FL2) to the flow direction before the bifurcation D1. The oscillations appear at some gauges that are specific to the gauge location. For instance, gauge P3 (see Figure 6(b)) located close to the entrance of the right floodplain shows more
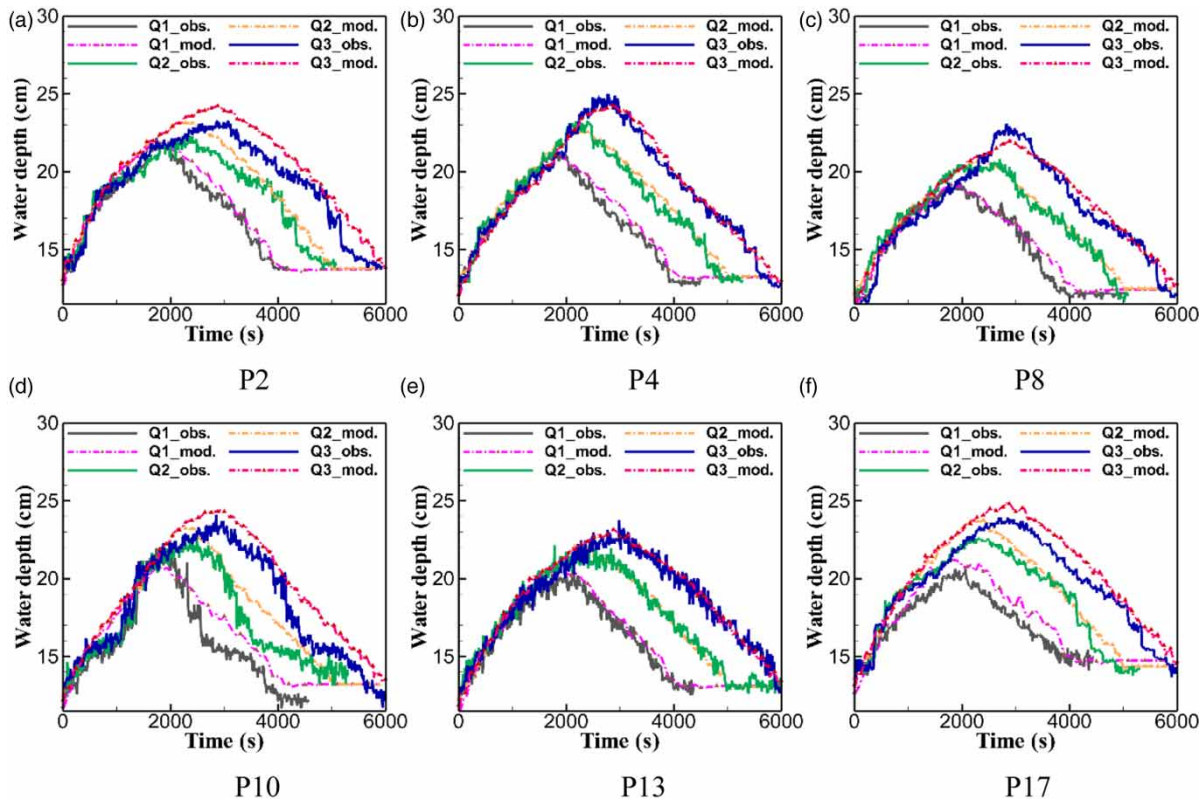
Figure 5 │ Comparison between modelled and observed flow depth evolution in the channels at the gauges (a) P2, (b) P4, (c) P8, (d) P10, (e) P13, and (f) P17 for the hydrographs Q1, Q2, and Q3.
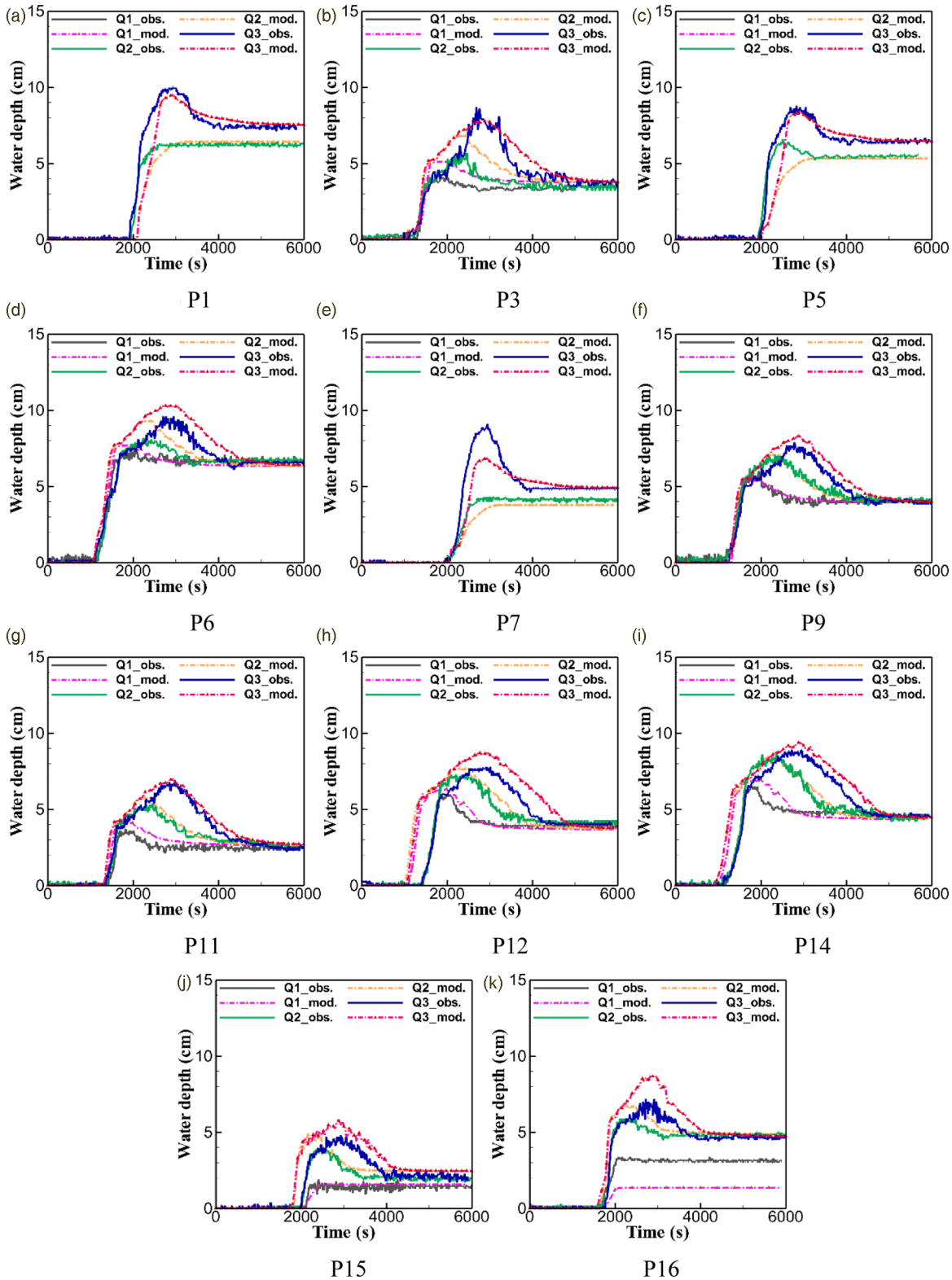
Figure 6 │ Comparison between modelled and observed flow depth evolution over the floodplains at the gauges (a) P1, (b) P3, (c) P5, (d) P6, (e) P7, (f) P9, (g) P11, (h) P12, (i) P14, (j) P15, and (k) P16 for the hydrographs Q1, Q2, and Q3.

pronounced oscillations that resulted from the flow interaction between the channel and floodplain. In addition, the flow interaction generates local flow circulation which travels on either side of the channel–floodplain interface. Likewise, some oscillations can be noticed at the gauges P6, P9, P11, and P16 (see Figure 6(d), 6(f), 6(g), and 6(k)), respectively. The possible reason could be the interaction of flow with the land boundary. Similarly, oscillations are seen at the gauges P12 and P14 (see Figure 6(h) and 6(i)) located on the island. In this case, local circulation takes place due to the channel–floodplain flow interaction from both sides of the island. On the contrary, water level profiles with no significant oscillations can be observed at the gauges P1, P5, and P7 (see Figure 6(a), 6(c), and 6(e)), respectively, located on the left floodplain (FL2) as the floodplain largely acts as storage.

Dynamic flood extent

The flood extents are extracted from the overlapped images at every 5 min interval using the visual interpretation technique. The full set-up is covered by five overlapping images. Each image is distorted to some extent at certain regions of the set-up. This is why they are geo-referenced and mosaicked to form a single image of the set-up. It is time-consuming to rectify all images one by one, and hence, we have followed a workflow in the geo-processing tool in the Arc-GIS platform to create a single image of the set-up. In the process, all the possible GCPs within the image are used for geo-referencing except the GCPs which fall under the water surface. The GCPs under water are difficult to accurately identify because of the refraction phenomenon. Subsequently, histogram equalization is separately performed on the mosaicked image to increase the contrast and visibility of the features. Several methods are available (Kaplan & Avdan 2017; Pradhan *et al.* 2017) to extract the features from the image. The water extent boundaries are tracked and digitized visually by tracing it along the water boundary through human interpretation and the process is known as visual interpretation technique. The potential of the visual interpretation technique to derive flooded area from the imageries is illustrated in some studies (Schumann *et al.* 2009; Stephens *et al.* 2012).

It is observed that some extra wet regions close to water boundaries are captured in the images because of ripples or waves. In addition, moving sunlight illumination and shadow of the nearby tree also produces specular and darker regions. Consequently, these regions pose great difficulty in classifying the flooded area. Therefore, in these regions, separate recordings are done to understand the spreading of water surface extent within a specific time interval. This step helps us to eliminate the erroneous object features that may have fallen in the water class. The extracted flood extents, i.e. inundation maps, overlaid on the ortho-image of the set-up are shown in Figures 7–9. Only a few maps are presented due to limited space.

It is obvious from Figures 7–9 that as the inflow rate increases in the rising limb, the amount of overbank flow at different locations increases and deluges the adjacent floodplains. Also, the inundation maps are quite irregular due to uneven bathymetry and changing flow dynamics. Similar maps cannot be reproduced by simply imagining a plane surface which passes through the channel water levels intersecting the DEM on the floodplain (Horritt & Bates 2001). These maps together with the time series of water elevation at different gauges for different flood scenarios can now be used for validating a variety of flood prediction models. The datasets can also be useful for various coupling algorithms used in 1D–2D (Bladé *et al.* 2012) and storage cell (Hunter *et al.* 2005) models.

Numerical simulations by TELEMAC 2D

Sensitivity analysis

In this section, the sensitivity of different types of advection schemes for solving the velocity and various turbulence models with a wide range of Manning's roughness coefficient (n) is examined for choosing a robust scheme and a turbulence model. A generalized wave equation is chosen in all the simulations because it is optimum in terms of CPU time. As mentioned above, three schemes are taken into account, namely the method of characteristics, SUPG, and edge-by-edge implementation of the upwind explicit finite volume method that are used for velocity. However, the recommended (default) mass-conservative scheme is used for the depth computation. The flood hazard maps,
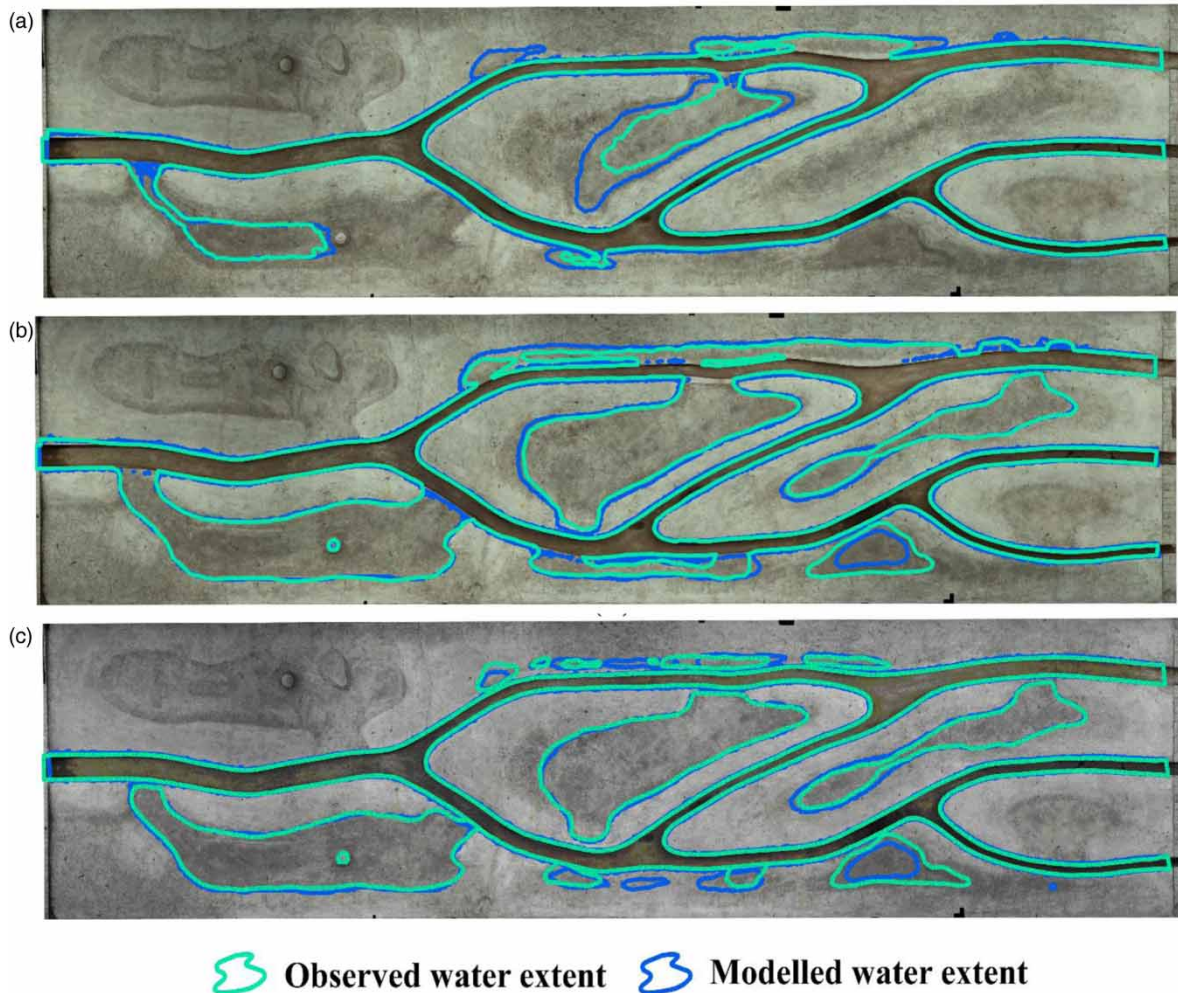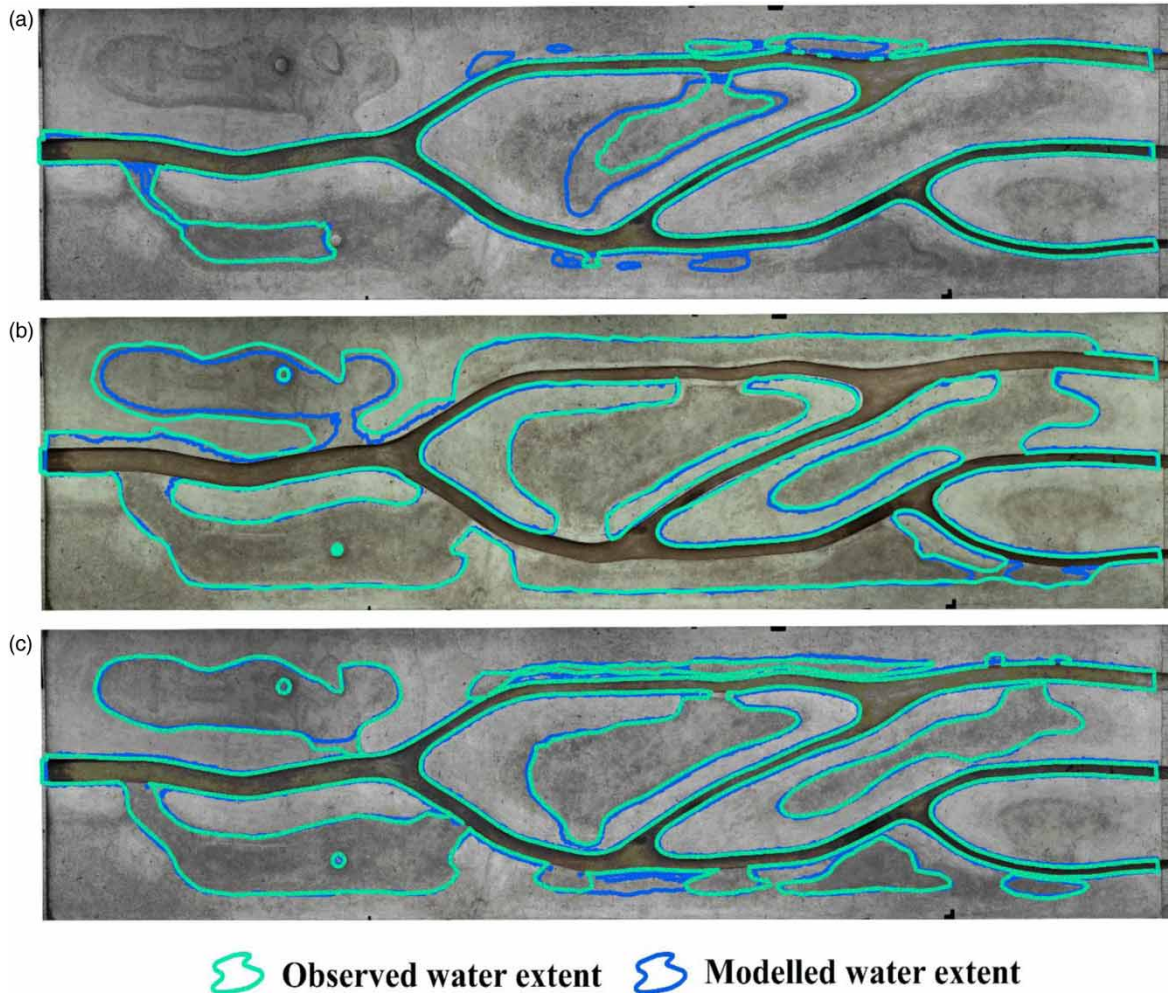
Figure 7 │ Flood inundation extents extracted using the visual interpretation technique for the Q1 hydrograph at the time instants (a) $t = 1,200$ s, (b) $t = 2,400$ s, and (c) $t = 3,600$ s.

in practice, are prepared with the help of the depth-averaged 2D flow models which do not incorporate a proper turbulence model (Arrault *et al.* 2016). Instead, all the dissipative effects are lumped into the friction term. However, our experimental data provides an opportunity to specifically test the influence of turbulence models together with the friction term on flood prediction. Three cases are considered for the sensitivity analysis of turbulence: (a) zero/no turbulence, (b) k–ε model, and (c) Smagorinsky model. Regarding the friction term, the n-value for smooth concrete is chosen within the range of 0.004–0.016 m$^{-1/3}$ s. A single n parameter value is taken for both the channel and floodplain as the set-up is made up of the same material and with similar kind of surface finishing.

The aforementioned advection schemes and turbulence models are tested for steady peak discharge of Q1 hydrograph, and the observations are summarized in Table 1.

The above-simulated results suggest that all the advection schemes are not providing similar predictions. Some of them were found to be overpredicting or resulted in unrealistic predictions as compared to the observed data. For instance, the method of characteristics for the computation of velocity with all the turbulence models provides excessive overprediction. It can also be seen that the edge-by-edge implementation of the upwind explicit finite volume method for velocity and the mass-conservative scheme for depth appear to be the best combination for achieving realistic results when combined with/without a

Observed water extent   **Modelled water extent**

Figure 8 │ Flood inundation extents extracted using the visual interpretation technique for the Q2 hydrograph at the time instants (a) $t = 1,200$ s, (b) $t = 2,400$ s, and (c) $t = 3,600$ s.

turbulence model in the given range of n-value. Thus, from Table 1, it can be concluded that the main contribution to the model outputs comes from the advection scheme. This analysis on steady-state discharge, therefore, helped us to select only the robust advection scheme to be used in the rest of the simulations. From this fact, the same combination is extended to the unsteady Q1 hydrograph for quantitative error analysis in order to evaluate the usefulness of turbulence models in flood simulations. The error analysis can be performed with respect to flood depth and extent.

First, the computed dynamic flow depths are compared with the observed flow depths at different gauges, and the error is estimated in terms of root-mean-square error (RMSE). Figure 10 illustrates the minimum RMSE obtained

for the combination of the n-value and the turbulence models at different gauges. The k–ε turbulence model is found to perform better for $n = 0.004$ m$^{-1/3}$ s at nine gauges. On the other hand, the Smagorinsky turbulence model and zero turbulence provide better accuracy for $n = 0.014$ m$^{-1/3}$ s at eight gauges and $n = 0.016$ m$^{-1/3}$ s at six gauges, respectively. However, the RMSE values for the k–ε turbulence model are notably higher than the other turbulence models. It is also found that a slight change in the n-value for the case of the k–ε turbulence model leads to the large variation in the RMSE. Thus, it can be said that the k–ε turbulence model is more sensitive to the n-value than the Smagorinsky turbulence model. It is also observed that the k–ε turbulence model needs more
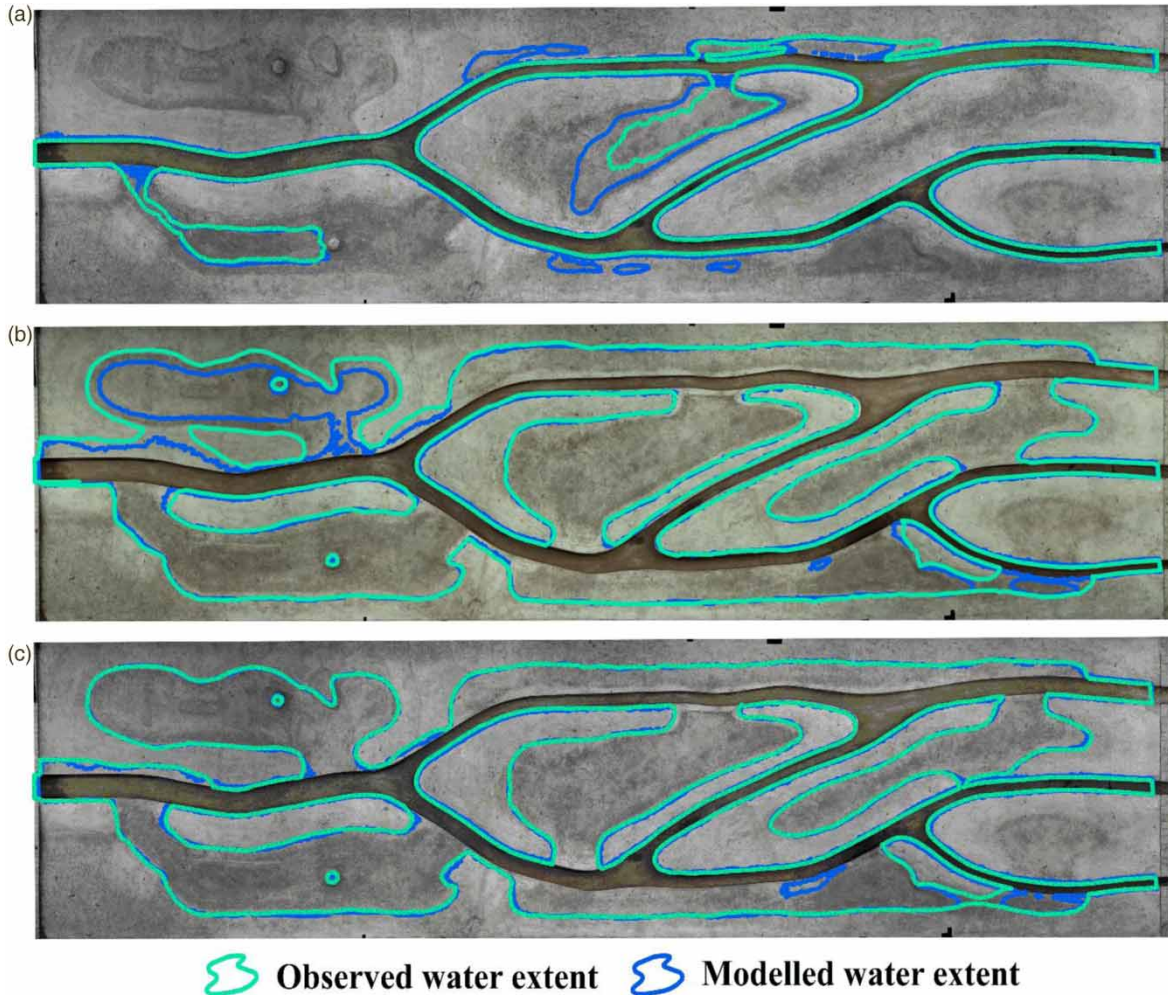
Figure 9 │ Comparison of flood inundation extents for the Q3 hydrograph at the time instants (a) $t = 1,200$ s, (b) $t = 2,400$ s, and (c) $t = 3,600$ s.

computation time (11.15 h) compared to the Smagorinsky turbulence model (6.30 h) and the zero turbulence model (5.10 h) for a complete simulation using a desktop computer with the following configuration: Processor – Intel®Xeon®, CPU E5 2630 v4 @2.20 GHz, RAM-64 GB, logical processor: 18, System type-64 bit. Hence, it can be stated that the inclusion of a different process in the turbulence model would give the different physical meaning of the surface roughness. It appears from the error analysis and computation time that the Smagorinsky model outperforms the k–ε model for the considered test cases. This analysis, thus, helps us to discard the k–ε turbulence model from further consideration. However, it cannot be confirmed only from this analysis whether a turbulence model is at all required for flood simulations.

Therefore, the error analysis is also performed with respect to the observed inundation extent (derived by visual interpretation) at different time intervals. The simulated inundation area is compared with the observed value, and the measure of fit (F) is evaluated by the function given below (Horritt & Bates 2001):

$$F = \frac{Num\ (S_{\mathrm{pred}}\ \cap\ S_{\mathrm{obs}})}{Num\ (S_{\mathrm{pred}}\ \cup\ S_{\mathrm{obs}})} \tag{4}$$

where S_{pred} and S_{obs} represent the sets of cells or the area or pixels classified as wet by the simulation and visual interpretation, respectively. The operator $Num\ (\cdot)$ gives a

Table 1 │ Summary of simulated results obtained with different numerical schemes and turbulence models for the range of n-value (0.004–0.016) m$^{-1/3}$ s

Type of advection scheme

Velocity (u and v)	Water depth (h)	Turbulence model	Results for n-value (0.004–0.016) m$^{-1/3}$ s
Method of characteristics	Mass-conservative scheme	No turbulence k–ε turbulence Smagorinsky	Excessive overpredictions for all the n
Centred semi-implicit scheme + SUPG	Mass-conservative scheme	No turbulence k–ε turbulence Smagorinsky	Spurious oscillations and overpredictions for all the n
Edge-by-edge implementation of the upwind explicit finite volume	Mass-conservative scheme	No turbulence k–ε turbulence Smagorinsky	Realistic predictions for all the n Realistic and slight overpredictions for higher n and computationally expensive Realistic predictions for all the n
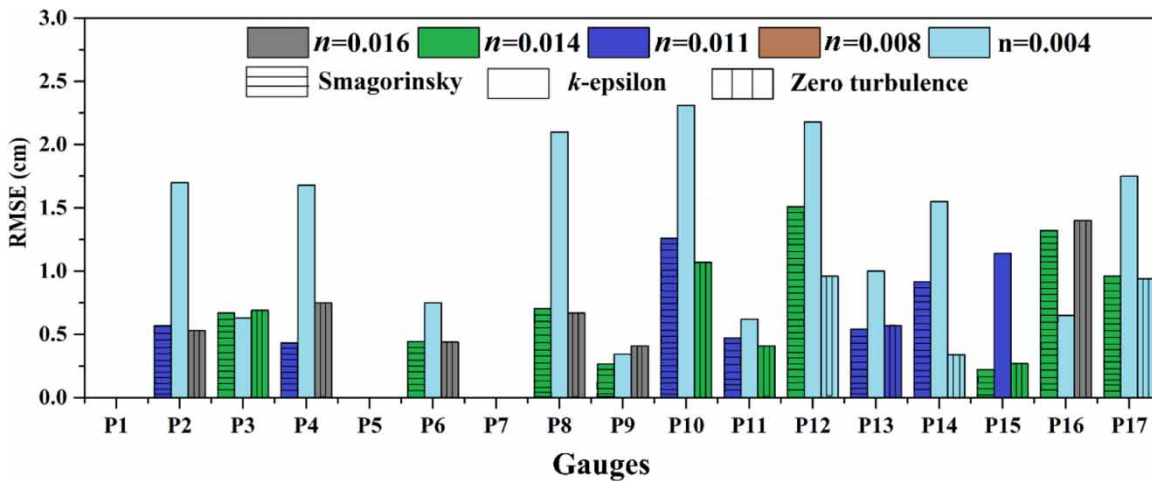
Figure 10 │ Minimum RMSE of water depth achieved during calibration of the TELEMAC 2D model for various n-values and turbulence models.

Table 2 │ Comparison of inundation extents through the measure of fit obtained from zero turbulence and Smagorinsky turbulence models

	Zero turbulence		Smagorinsky		
Time interval (min)	F	Area (m²)	F	Area (m²)	Observed area (m²)
20	0.73	19.77	0.76	20.53	16.16
30	0.87	33.40	0.88	33.75	33.23
40	0.84	31.89	0.83	33.15	29.3
50	0.84	27.24	0.85	29.03	27.3
Maximum inundation	0.89	33.57	0.95	35.49	37.15

number of members of the set. The function F shows the performance of the algorithm for classification as the range can lie between $F = 1$ for a perfect prediction and $F = 0$ for no region being correctly predicted with respect to the observed data.

Table 2 provides the comparison of F-values and it appears that the accuracy improves when the Smagorinsky model is used. However, the difference in accuracy for no turbulence and with the turbulence model is found to be insignificant. However, further investigations on the dynamic inundation maps show that though the computations without a turbulence model predict a similar

F-value for a test run, the simulated dynamic inundation patterns are slightly different than the observed ones. The model with no turbulence predicts the dry area as wet and overpredicts the wet area in some regions. Conversely, the Smagorinsky model predicts the inundation extent very similar to that of the observed one at all time intervals and for all cases. Therefore, the Smagorinsky turbulence model with $n = 0.014\,\mathrm{m}^{-1/3}\,\mathrm{s}$ is chosen here for all the simulations.

Comparison of simulation results

This section investigates the accuracy of the numerical model considering a number of aspects such as wave arrival time, time to peak, maximum water depth, inundation area, and its measure of fit. Figures 5 and 6 illustrate the comparisons between modelled and observed water levels in the channels and on the floodplains, respectively, for the three cases. It can be seen from the figures that some of the features of the water levels are well modelled, notably, following the similar patterns of the observed data. However, at a few locations within the channels, the model overpredicts the water levels. The overprediction is found at the locations where water overflows onto the floodplains, and in the vicinity of the bifurcations and junction. For examples, P2, P10, and P17 gauges (see Figure 5(a), 5(d), and 5(f)) show higher peak water levels, respectively. At P8 gauge (see Figure 5(c)), the peak water level is well predicted for low inflows, but for the higher inflow, i.e. for the third case, the peak is underpredicted. The variations may be attributed to the complex flow dynamics at a channel–floodplain interface and at bifurcation. The flow at these locations is 3D in nature on account of the lateral and vertical exchange of momentum between the flow layers and dominant secondary circulation. These features linked to the vertical velocity component are completely absent in the 2D model. On the other hand, it can be noted that the same model is able to simulate similar peaks at other locations in the channels where the flow dynamics is relatively simple, for example, at P4 and P13 gauges (see Figure 5(b) and 5(e)), respectively. The above comparisons prove that the 2D model may be further improved as far as river–floodplain interaction, bifurcation, and junction hydraulics are concerned, and our

experimental observations may serve as benchmarking datasets in this direction.

Overall, the pattern of water levels at different gauges is reasonably well predicted. However, some gauges (P1, P12, P14, and P15) exhibit discrepancies in modelling the water level changes (see Figure 6). On the other hand, it appears that the modelled wavefronts are closely conforming to the observed values at some gauges (P3, P6, P9, and P16), as shown in Figure 6. On the left floodplain, the arrival of the modelled waterfront is delayed at all the gauges (P1, P5, and P7), as shown in Figure 6, which suggests that overflow onto the floodplain is delayed. This can be confirmed by looking at underpredicted water level at gauge P8 (see Figure 5(c)). This might be due to the inability of the model to capture the weak hydraulic jump formed at the upstream of bifurcation D1, and hence, the water level gets affected at P8. Our close observation during the experiments shows that due to the obstruction of flow at bifurcation D1, water heads up in the main upstream channel and forms the weak hydraulic jump. It is also noticed that the 2D model does not have the capability to capture the temporal fluctuation generated from the reflection of waves by the solid surface, for example, more pronounced fluctuation observed at P3 (see Figure 6(b)). Further details regarding the time of water wave advancing to the various gauges are compared in Figure 11.

It is important to know that maximum damages during a flood could be expected during the time at which maximum flow depth occurs. Hence, the maximum flow depths predicted by the model at various locations are compared to those observed, as depicted in Figure 12. Except at a few gauges (P13, P14, and P15), the predicted time of peak at all the gauges are seen to closely match the observed values for the hydrograph Q1. For Q2, the predicted time of peak is observed to vary more in comparison to the observed data at most of the gauges (see Figure 12). Conversely, for Q3, the time of peak at all the gauges is quite close to the observed values.

The performance of the model is evaluated by computing the RMSE of water depths at all the stations against the observed data (see Figure 13). The maximum RMSE occurs at location P12, followed by P10 for all the cases. This is because P10 is located just after the bifurcation D1, where the flow is predominantly 3D, and hence, the 2D
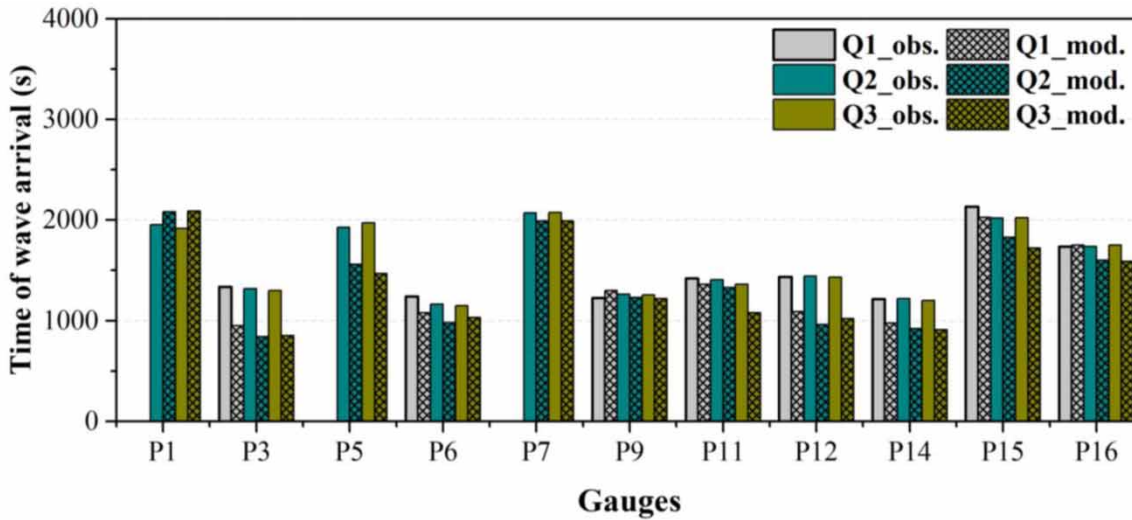
Figure 11 │ Comparison between modelled and observed times of water wave arrival at various gauges over the floodplains.

model shows a higher discrepancy. In addition, two distinct separation zones are observed in the main channel and just after the station P10. Also, water from the right floodplain is disposed into the channel near the P10 gauge, and the flow gets affected. For gauge P12 located on the island, the simulated flood front arrives before the observed time, and hence, the RMSE is higher compared to the rest of the stations. However, the RMSE values at most of the stations remain within the range of 0–1 cm.

In terms of inflow hydrograph, a higher inflow discharge leads to higher RMSE at most of the stations. This might be due to the increase in the Froude number and the solution scheme in TELEMAC 2D may not be robust enough to handle such flow.

Flood extent analysis

Figures 7–9 depict the comparison between modelled and observed flood inundation extents for Q1, Q2, and Q3 hydrographs, respectively. At $t = 1{,}200$ s, the model seems to overpredict the flood extents for all the cases. However, the model is able to simulate similar flood extents during the passage of the peak of the hydrographs. Thus, it can be understood that the model fails to capture the actual entry of the waterfront over the floodplain at the initial stage and also the advancement of the waterfront. The possible reason for overprediction may be attributed to the 2D

model which does not take vertical velocity component into account, and thus, the formation of eddies and vortices in the process is neglected. As a consequence, the right amount of energy loss would not occur which may change the flow dynamics to a certain extent. However, this may be compensated by using spatially varying Manning's n, but such an approach needs rigorous calibration through iterations.

The comparisons between the simulated and observed areas of inundation for different flood hydrographs are shown in Figure 14. It can be observed that the model, in general, slightly overpredicts inundation extent during the rising limb and underpredicts during the falling limb of the hydrographs. It suggests that the simulated flood water rushes faster than the observed one during the rising limb of the hydrographs. This phenomenon can be seen in the recorded movement of the water front at the gauges P12, P14, P15, and P16 (see Figure 6) located over floodplains (FL1) and the island (IS1, IS2). As a result, more area than the observed one is inundated during the rising limb (see Figures 8–10). Conversely, the simulated flood water recedes faster than the observed one during the falling limb of the hydrographs. The reduction in simulated and observed water depths are recorded at the gauges P1, P5, P7, P3, P11, P12, and P14 (see Figure 6) located over flood-plains (FL1, FL2) and the island (IS1). As a result, the simulated inundation extent appears to be marginally
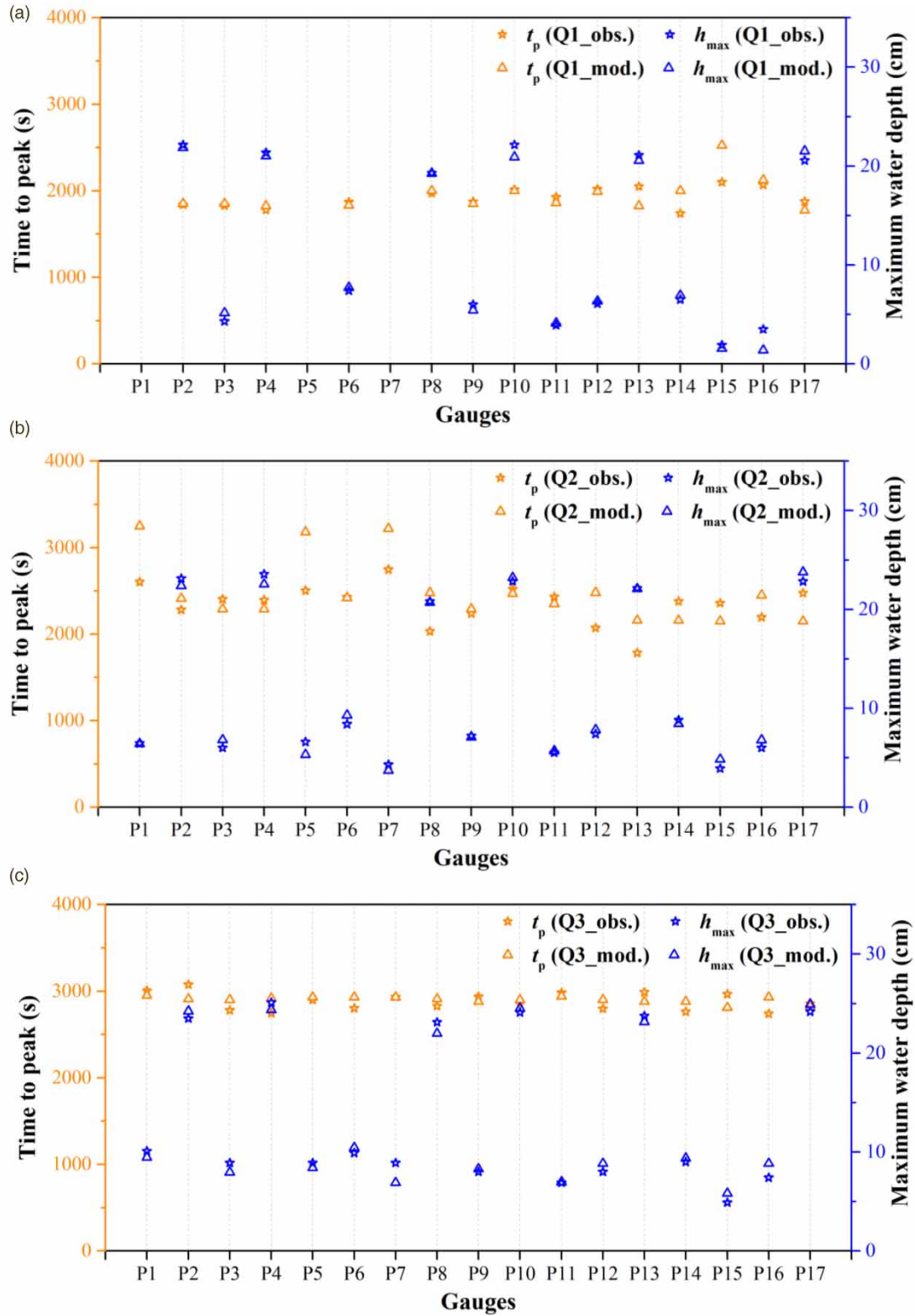
Figure 12 │ Comparison between modelled and observed maximum flow depths (h_{max}) and their peak times (t_p) at the various gauges for the hydrographs (a) Q1, (b) Q2, and (c) Q3.

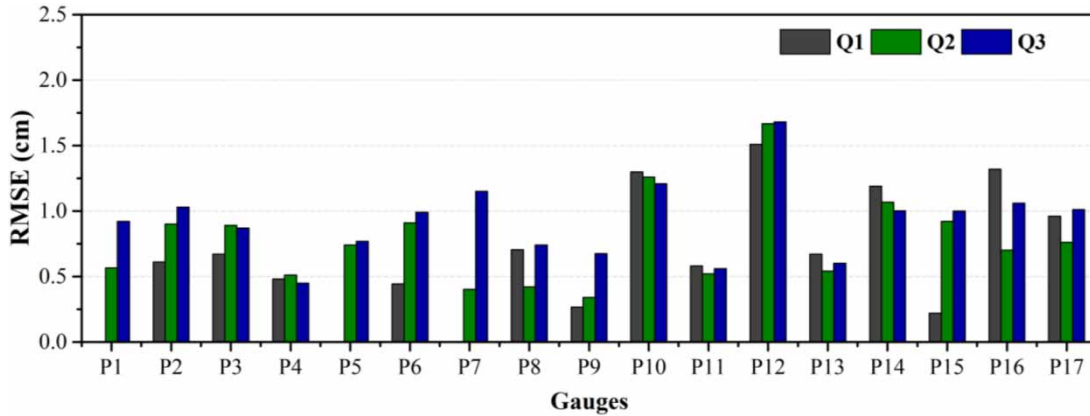**Figure 13** │ RMSE (cm) of water depth calculated between modelled and observed data for the hydrographs Q1, Q2, and Q3.
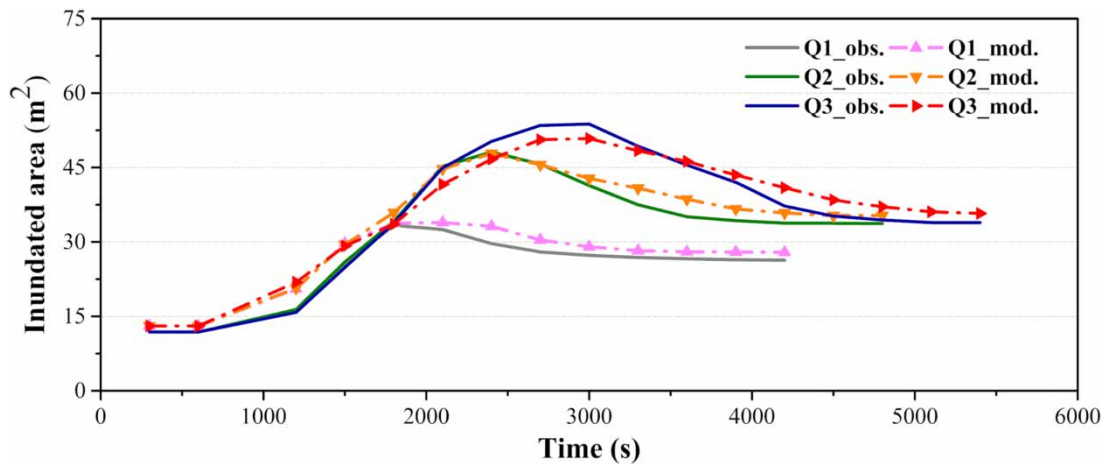

Figure 14 │ Comparison between modelled and observed inundation areas for the hydrographs Q1, Q2, and Q3.

underpredicting than the observed extent during the falling limb of the hydrographs (see Figures 8–10).

Figure 15 compares the F-values derived from all the cases for different time intervals. One can easily observe that the absolute value of F differs with the time interval. The accuracy of inundation extent using the F-test is satisfactory ($F > 0.75$). With the exception of overprediction at $t = 1{,}200$ s, which is due to overspreading of water on the floodplains at the initial stage, at all other times the accuracy of the simulated flood extents is found to be exceptionally good ($F > 0.83$) for all the cases.

From the simulation results, it can be noted that the model is able to satisfactorily reconstruct the unsteady-state flood experiments. Also, it is evident from the results that the TELEMAC 2D model is able to reproduce

experimental flood events conducted in a channel-network-floodplain set-up provided suitable hydrodynamic and turbulent model combination is used for simulations.

Maximum inundation extent

The maximum inundation extent is often required for issuing flood warning, preparing hazard maps, and carrying out damage analysis. For this purpose, the observed maximum inundation extents are examined by analysing each experiment through the images for the entire flood duration. The computed maximum inundation extents are also extracted using the same approach and are compared in Figure 16. The observed and simulated maximum inundation areas are 37.15 and 35.49 m^2, 50.91 and 48.62 m^2,
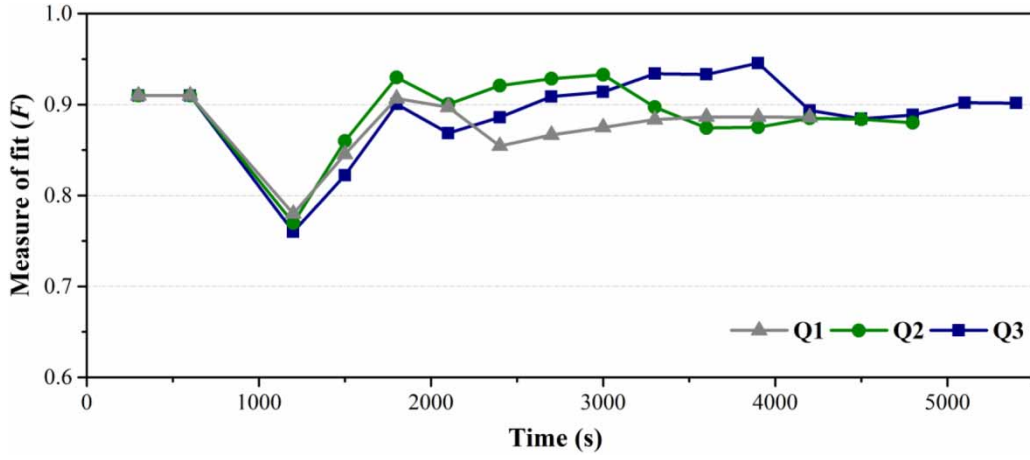
Figure 15 │ Comparison of the measure of fit (*F*) derived for the hydrographs Q1, Q2, and Q3.
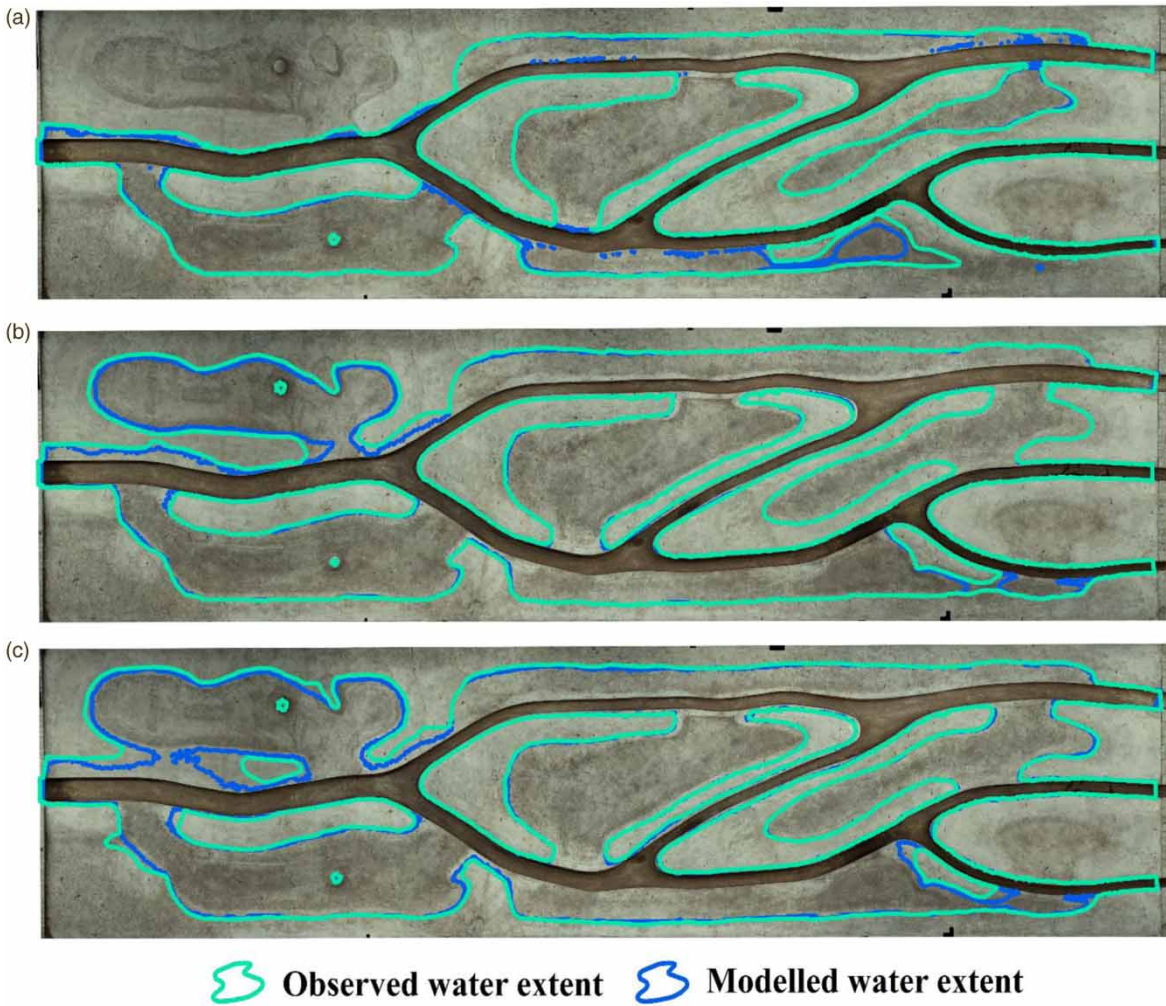

Figure 16 │ Maximum inundation extents observed during the flood events for the hydrographs (a) Q1, (b) Q2, and (c) Q3.

and 54.92 and 51.29 m^2 for Q1, Q2, and Q3, respectively. The F-test is also performed against the observed data and the values of 0.95, 0.96, and 0.94 are obtained for Q1, Q2, and Q3, respectively. It is to be noted that although the inundation areas predicted by simulations and those observed are quite close, the model, overall, underpredicts the maximum inundation extent for all the cases.

From this analysis, it can also be stated that the accuracy of maximum inundation prediction is surprisingly higher than that at different time intervals (see Dynamic flood extent). Hence, it can be concluded that for a comprehensive evaluation of the accuracy of a model, it is necessary that the model should be tested not only for maximum inundation extents, but also for dynamic inundation extents. Moreover, the simulated flow depths have to be validated to take care of the unsteady nature of flood dynamics. The rigorous comparison of experimental observations and numerical results presented in this study ensures the quality of the generated datasets.

CONCLUSIONS

This study describes the experimental procedure and acquisition of datasets on flood dynamics in a river-network-floodplain set-up. The datasets comprise high-resolution topography of the set-up, time series of flow depth evolution, flood arrival time, and time to peak, dynamic flood extents, maximum flood extent, and boundary conditions for mathematical models. The datasets are generated by passing stepped hydrographs through the channel-network and recording the dynamic fluvial floods. During each run, the evolution of flow depths at various locations is recorded using ultrasonic sensors. The flood extents at different time intervals are extracted by processing the overlapped images of the set-up using the visual interpretation technique. Apart from data collection, the TELEMAC 2D model is applied to mathematically reconstruct the experimental floods. A number of solution schemes with or without various turbulence models are tried for assessing the best alternative. The sensitivity analysis of different numerical schemes and turbulence models established that the scheme which uses edge-by-edge implementation of the upwind explicit finite volume discretization for

advection of velocity and mass-conservative scheme for depth together with the Smagorinsky turbulence model is capable of reproducing the experimental flooding events with higher accuracy. Inclusion of the turbulence model is found to influence the accuracy in predicting dynamic flood extents. The 2D model overpredicts inundation extents during the rising limb of the hydrographs and underpredicts during the falling limb. This indicates that the model is not able to capture the wave propagation accurately over the floodplain. It is important to note that in the vicinity of bifurcations, junction, and overflow locations, the flow dynamics are quite complex and the accuracy of the 2D model in replicating the largely 3D flow field is undermined. Therefore, the experimental datasets can play a significant role in improving 2D flow models for more accurate flood prediction in the future. In addition, the datasets on flood dynamics can be utilized as an alternative to satellite imageries to evaluate the performance of flow models. The datasets are freely downloadable.

ACKNOWLEDGEMENTS

FUNDING

DATA AVAILABILITY

In this paper, three unsteady experimental datasets on floods are generated to validate mathematical models. These datasets include the DEM, time-varying flow depths at various locations, dynamic inundation extents, and the maximum inundation extents. The datasets are freely downloadable at the given link: https://www.hydroshare.org/resource/e5a28a1c273641ff9d4b334fd2d06580/. The datasets should be used for academic purposes.

REFERENCES

Abderrezzak, K. E. K., Paquier, A. & Mignot, E. 2009 Modelling flash flood propagation in urban areas using a two-dimensional numerical model. *Natural Hazards* **50** (3), 433–460. https://doi.org/10.1007/s11069-008-9300-0.

Arrault, A., Finaud-Guyot, P., Archambeau, P., Bruwier, M., Erpicum, S., Pirotton, M. & Dewals, B. 2016 Hydrodynamics of long-duration urban floods: experiments and numerical modelling. *Natural Hazards and Earth System Sciences* **16** (6), 1413–1429. https://doi.org/10.5194/nhess-16-1413-2016.

Barthélémy, S., Ricci, S., Morel, T., Goutal, N., Le Pape, E. & Zaoui, F. 2018 On operational flood forecasting system involving 1D/2D coupled hydraulic model and data assimilation. *Journal of Hydrology* **562** (5), 623–634. https://doi.org/10.1016/j.jhydrol.2018.05.007.

Bhola, P. K., Nair, B. B., Leandro, J., Rao, S. N. & Disse, M. 2019 Flood inundation forecasts using validation data generated with the assistance of computer vision. *Journal of Hydroinformatics* **21** (2), 240–256. https://doi.org/10.2166/hydro.2018.044.

Bladé, E., Gómez-Valentín, M., Dolz, J., Aragón-Hernández, J. L., Corestein, G. & Sánchez-Juny, M. 2012 Integration of 1D and 2D finite volume schemes for computations of water flow in natural channels. *Advances in Water Resources* **42**, 17–29. https://doi.org/10.1016/j.advwatres.2012.03.021.

Blazek, J. 2015 *Computational Fluid Dynamics: Principles and Applications*. Butterworth-Heinemann, Oxford.

Brooks, A. N. & Hughes, T. J. 1982 Streamline upwind/Petrov-Galerkin formulations for convection dominated flows with particular emphasis on the incompressible Navier-Stokes equations. *Computer Methods in Applied Mechanics and Engineering* **32** (1–3), 199–259.

Defina, A. & Bixio, A. C. 2005 Mean flow and turbulence in vegetated open channel flow. *Water Resources Research* **41** (7), 1–12. https://doi.org/10.1029/2004WR003475.

Di Baldassarre, G., Schumann, G. & Bates, P. D. 2009 A technique for the calibration of hydraulic models using uncertain satellite observations of flood extent. *Journal of Hydrology* **367** (3–4), 276–282. https://doi.org/10.1016/j.jhydrol.2009.01.020.

Eltner, A., Kaiser, A., Castillo, C., Rock, G., Neugirg, F. & Abellán, A. 2016 Image-based surface reconstruction in geomorphometry-merits, limits and developments. *Earth Surface Dynamics* **4** (2), 359–389. https://doi.org/10.5194/esurf-4-359-2016.

Giustarini, L., Vernieuwe, H., Verwaeren, J., Chini, M., Hostache, R., Matgen, P. & De Baets, B. 2015 Accounting for image uncertainty in SAR-based flood mapping. *International Journal of Applied Earth Observation and Geoinformation* **34** (1), 70–77. https://doi.org/10.1016/j.jag.2014.06.017.

Hervouet, J. M. 2007 *Hydrodynamics of Free Surface Flows: Modelling with the Finite Element Method*, Vol. 360. Wiley, New York.

Hervouet, J. M. 2013 The weak form of the method of characteristics, an amazing advection scheme. In: *XXth TELEMAC-MASCARET*. User Conference, pp. 1–6.

Hervouet, J. M., Razafindrakoto, E. & Villaret, C. 2011 Dealing with dry zones in free surface flows: a new class of advection schemes. In: *Proceedings of the 34th World Congress of the International Association for Hydro-Environment Research and Engineering: 33rd Hydrology and Water Resources Symposium and 10th Conference on Hydraulics in Water Engineering*. Engineers Australia, Australia, p. 4103.

Hervouet, J. M. & Van Haren, L. 1996 Recent advances in numerical methods for fluid flows. In: *Floodplain Processes* (M. G. Anderson, D. E. Walling & P. D. Bates, eds). John Wiley & Sons, Chichester, pp. 183–214.

Horritt, M. S. & Bates, P. D. 2001 Effects of spatial resolution on a raster based model of flood flow. *Journal of Hydrology* **253** (1–4), 239–249. https://doi.org/10.1016/S0022-1694(01)00490-5.

Horritt, M. S. & Bates, P. D. 2002 Evaluation of 1D and 2D numerical models for predicting river flood inundation. *Journal of Hydrology* **268** (1–4), 87–99. https://doi.org/10.1016/S0022-1694(02)00121-X.

Hunter, N. M., Bates, P. D., Horritt, M. S., De Roo, A. P. J. & Werner, M. G. F. 2005 Utility of different data types for calibrating flood inundation models within a GLUE framework. *Hydrology and Earth System Sciences* **9** (4), 412–430. https://doi.org/10.5194/hess-9-412-2005.

Kampf, S., Strobl, B., Hammond, J., Anenberg, A., Etter, S., Martin, C., Puntenney-Desmond, K., Seibert, J. & van Meerveld, I. 2018 Testing the waters: mobile apps for crowdsourced streamflow data. *Eos* **99**. doi:10.1029/2018EO096355.

Kaplan, G. & Avdan, U. 2017 Object-based water body extraction model using Sentinel-2 satellite imagery. *European Journal of Remote Sensing* **50** (1), 137–143. https://doi.org/10.1080/22797254.2017.1297540.

Mali, V. K. & Kuiry, S. N. 2018 Assessing the accuracy of high-resolution topographic data generated using freely available packages based on SfM-MVS approach. *Measurement* **124**, 338–350. https://doi.org/10.1016/j.measurement.2018.04.043.

Mali, V. K. & Kuiry, S. N. 2020 Experimental and numerical study of flood in a river-network-floodplain set-up. *Journal of Hydraulic Research*, 1–19. https://doi.org/10.1080/00221686.2019.1698471.

Martins, R., Leandro, J., Chen, A. S. & Djordjević, S. 2017 A comparison of three dual drainage models: shallow water vs local inertial vs diffusive wave. *Journal of Hydroinformatics* **19** (3), 331–348. https://doi.org/10.2166/hydro.2017.075.

Merwade, V., Cook, A. & Coonrod, J. 2008 GIS techniques for creating river terrain models for hydrodynamic modeling and flood inundation mapping. *Environmental Modelling & Software* **23** (10–11), 1300–1311. https://doi.org/10.1016/j.envsoft.2008.03.005.

Nicholson, J., Broker, I., Roelvink, J. A., Price, D., Tanguy, J. M. & Moreno, L. 1997 Intercomparison of coastal area

morphodynamic models. *Coastal Engineering* **31** (1–4), 97–123. https://doi.org/10.1016/S0378-3839(96)00054-3.

Pradhan, B., Sameen, M. I. & Kalantar, B. 2017 Optimized rule-based flood mapping technique using multitemporal RADARSAT-2 images in the tropical region. *IEEE Journal of Selected Topics in Applied Earth Observations and Remote Sensing* **10** (7), 3190–3199. https://doi.org/10.1109/JSTARS.2017.2676343.

Qian, H., Cao, Z., Liu, H. & Pender, G. 2018 New experimental dataset for partial dam-break floods over mobile beds. *Journal of Hydraulic Research* **56** (1), 124–135. https://doi.org/10.1080/00221686.2017.1289264.

Sanyal, J. 2017 Uncertainty in levee heights and its effect on the spatial pattern of flood hazard in a floodplain. *Hydrological Sciences Journal* **62** (9), 1483–1498. https://doi.org/10.1080/02626667.2017.1334887.

Sanyal, J., Carbonneau, P. & Densmore, A. L. 2014 Low-cost inundation modelling at the reach scale with sparse data in the Lower Damodar River basin, India. *Hydrological Sciences Journal* **59** (12), 2086–2102. https://doi.org/10.1080/02626667.2014.884718.

Schumann, G., Di Baldassarre, G. & Bates, P. D. 2009 The utility of spaceborne radar to render flood inundation maps based on multialgorithm ensembles. *IEEE Transactions on Geoscience and Remote Sensing* **47** (8), 2801–2807. https://doi.org/10.1109/TGRS.2009.2017937.

Shiono, K., Chan, T. L., Spooner, J., Rameshwaran, P. & Chandler, J. H. 2009 The effect of floodplain roughness on flow structures, bedforms and sediment transport rates in meandering channels with overbank flows: part II. *Journal of Hydraulic Research* **47** (1), 20–28. https://doi.org/10.3826/jhr.2009.2944-II.

Smith, M. W., Carrivick, J. L., Hooke, J. & Kirkby, M. J. 2014 Reconstructing flash flood magnitudes using 'Structure-from-Motion': a rapid assessment tool. *Journal of Hydrology* **519**, 1914–1927. https://doi.org/10.1016/j.jhydrol.2014.09.078.

Soares-Frazão, S. 2007 Experiments of dam-break wave over a triangular bottom sill. *Journal of Hydraulic Research* **45** (suppl.), 19–26. https://doi.org/10.1080/00221686.2007.9521829.

Soares-Frazão, S. & Zech, Y. 2007 Experimental study of dam-break flow against an isolated obstacle. *Journal of Hydraulic Research* **45** (suppl.), 27–36. https://doi.org/10.1080/00221686.2007.9521830.

Soares-Frazão, S., Lhomme, J., Guinot, V. & Zech, Y. 2008 Two-dimensional shallow-water model with porosity for urban flood modelling. *Journal of Hydraulic Research* **46** (1), 45–64. https://doi.org/10.1080/00221686.2008.9521842.

Stark, J., Plancke, Y., Ides, S., Meire, P. & Temmerman, S. 2016 Coastal flood protection by a combined nature-based and engineering approach: modeling the effects of marsh geometry and surrounding dikes. *Estuarine, Coastal and Shelf Science* **175**, 34–45. https://doi.org/10.1016/j.ecss.2016.03.027.

Stephens, E. M., Bates, P. D., Freer, J. E. & Mason, D. C. 2012 The impact of uncertainty in satellite data on the assessment of flood inundation models. *Journal of Hydrology* **414**, 162–173. https://doi.org/10.1016/j.jhydrol.2011.10.040.

Teng, J., Jakeman, A. J., Vaze, J., Croke, B. F. W., Dutta, D. & Kim, S. 2017 Flood inundation modelling: a review of methods, recent advances and uncertainty analysis. *Environmental Modelling & Software* **90**, 201–216. https://doi.org/10.1016/j.envsoft.2017.01.006.

Testa, G., Zuccalà, D., Alcrudo, F., Mulet, J. & Soares-Frazão, S. 2007 Flash flood flow experiment in a simplified urban district. *Journal of Hydraulic Research* **45** (suppl.), 37–44. https://doi.org/10.1080/00221686.2007.9521831.

Weber, L. J., Schumate, E. D. & Mawer, N. 2001 Experiments on flow at a 900 open-channel junction. *Journal of Hydraulic Engineering* **127** (5), 340–350.

Wormleaton, P. R. & Merrett, D. J. 1990 An improved method of calculation for steady uniform flow in prismatic main channel floodplain sections. *Journal of Hydraulic Research* **28** (2), 157–174.

Wormleaton, P. R., Sellin, R. H. J., Bryant, T., Loveless, J. H., Hey, R. D. & Catmur, S. E. 2004 Flow structures in a two-stage channel with a mobile bed. *Journal of Hydraulic Research* **42** (2), 145–162. https://doi.org/10.1080/00221686.2004.9628300.

Zeng, J., Constantinescu, G., Blanckaert, K. & Weber, L. 2008 Flow and bathymetry in sharp open-channel bends: experiments and predictions. *Water Resources Research* **44** (5). https://doi.org/10.1029/2007WR006303.

Zheleznyakov, G. V. 1971 Interaction of channel and floodplain streams. In: *Proceedings of the 14th LAHR Congress*, Paris, Vol. 5, pp. 145–148.